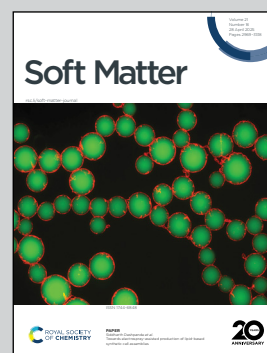**Highlighting the research from the Micro & Nanoscale Transport (MNT) Laboratory at the University of Waterloo, Canada, led by Professor Sushanta K. Mitra.**

Magnetic manipulation of liquid-wrapped hydrogels

A magneto-responsive hydrogel–liquid suspension interacts with a floating liquid interfacial layer on a water bath, undergoing interfacial penetration to form magneto-responsive cargos. This research explores the underlying mechanism and demonstrates its effectiveness in underwater magnet-assisted manipulation.

Image reproduced by permission of Sushanta Mitra from *Soft Matter*, 2025, **21**, 2994.

ROYAL SOCIETY
OF **CHEMISTRY**

rsc.li/soft-matter-journal

PAPER

Check for updates

Magnetic manipulation of liquid-wrapped hydrogels†

Utsab Banerjee, Sirshendu Misra [iD] and Sushanta K. Mitra [iD]*

This study explores the encapsulation of magnetic and non-magnetic hydrogels within a liquid medium using the liquid–liquid encapsulation technique. The encapsulation process involves the suspension of hydrogels in laser oil, followed by the generation of compound core droplets, which are then wrapped by an interfacial layer of canola oil floating on a water bath. This method produces magneto-responsive compound encapsulated cargos with potential applications in diverse fields such as drug delivery, tissue engineering, and soft robotics. The magnetic properties of these encapsulated cargos are exploited for magnet-assisted release and underwater manipulation, demonstrating enhanced stability, controlled release, and adaptability. This research opens new avenues for the application of magnetic hydrogels in dynamic and responsive systems.

1. Introduction

Encapsulation is a versatile technique with broad applicability across various industries, including pharmaceuticals/nutraceuticals,[1] agriculture,[2] food processing,[3,4] cosmetics,[5] aroma therapy,[6] and electronics.[7] Its primary purpose is to protect and control the release of active materials by enclosing them – referred to as the "core" – within a protective "shell."[8,9] This versatility is demonstrated by the fact that depending on the application, the core can exist in solid, liquid, or gas form, while the shell should be a solid or liquid phase, possessing key properties such as strength, stability, and impermeability.[10,11] This broad applicability and potential of encapsulation techniques make it a significant area of research in various fields.

Magnetic nanoparticles (MNPs) have emerged as a crucial component in biomedical applications due to their unique chemical composition, morphology, and magnetic properties.[12,13] These nanoparticles are extensively used in targeted drug delivery,[14–17] magnetic hyperthermia,[18,19] and magnetic resonance imaging (MRI).[20,21] The ferrofluids are the stable colloidal suspensions of these MNPs (~ 10 nm) that exhibit superparamagnetic behaviour and respond to external magnetic fields.[22–24] Studies have explored ferrofluid encapsulation inside liquid or polymer to enhance stability and functionality,[25,26] yet limited attention is given to incorporating ferrofluids inside a hydrogel.

Hydrogels, as three-dimensional, water-swollen polymer networks, are recognized for their biocompatibility, tunable

properties, and wide applications in tissue engineering,[27–29] drug delivery,[28,29] and cell encapsulation.[30] However, conventional hydrogels have some drawbacks, such as limited controllability, inadequate actuation capabilities, and passive diffusion-driven release mechanisms.[31,32] These limitations hinder their effectiveness in applications demanding precise and controlled delivery of biological agents or drugs. To address these shortcomings, magnetic hydrogels have gained attention due to their enhanced responsiveness to external magnetic fields and their potential to improve controlled delivery and actuation.[31,33–35] Magnetic hydrogels, composed of a polymer matrix embedded with MNPs, are increasingly recognized for their biocompatibility, flexibility, and responsiveness to magnetic fields. The literature indicates that the primary focus remains on magnetic hydrogel synthesis using microfluidic platforms,[36,37] magnetic hydrogel-based actuators,[38] and drug and cell encapsulation inside the hydrogel.[19,30]

Despite these advancements, the encapsulation of magnetic hydrogels within a liquid medium still needs to be explored. Encapsulation of magnetic hydrogels in liquids offers several key advantages. First, it enhances the stability of the encapsulated material by reducing exposure to environmental factors such as oxidation, moisture, or temperature fluctuations. This ensures the longevity and efficacy of sensitive bioactive compounds. Second, the liquid medium enables controlled release of the encapsulated material, allowing precise delivery of active agents at targeted sites over a desired timeframe. This feature is particularly valuable in drug delivery and other biomedical applications where dose accuracy is critical. Third, encapsulation in liquids protects delicate bioactive substances, such as enzymes, proteins, or therapeutic agents, from degradation during storage or transport. This protective environment maintains their functional integrity and effectiveness. Finally, the presence of a liquid medium allows for the modulation of mechanical

Micro & Nano-scale Transport Laboratory, Waterloo Institute for Nanotechnology, Department of Mechanical and Mechatronics Engineering, University of Waterloo, 200 University Avenue West, Waterloo, Ontario N2L 3G1, Canada.
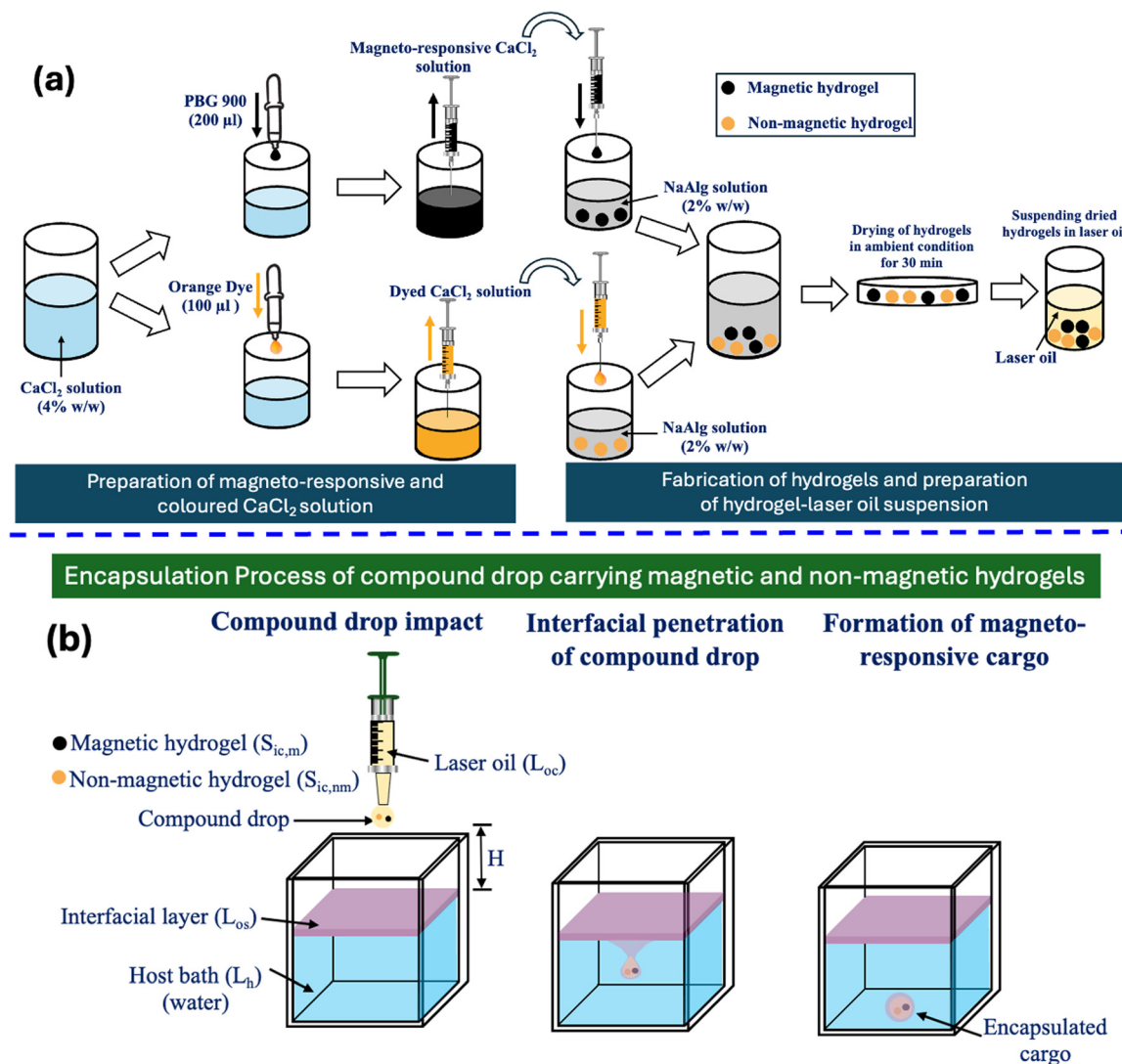*E-mail: skmitra@uwaterloo.ca*

Fig. 1 (a) The schematic depicting the preparation of magneto-responsive and coloured calcium chloride (CaCl$_2$) solution (4% w/w), the fabrication of the magnetic and non-magnetic hydrogels and the preparation of the hydrogel-laser oil suspension. (b) The schematic of the encapsulation framework involves the impact-driven wrapping of a compound core drop consisting of laser oil (L_{oc}) carrying a magnetic ($S_{ic,m}$) and non-magnetic ($S_{ic,nm}$) hydrogel by an interfacial layer (L_{os}-canola oil) floating on the host water bath (L_h). The impact height (H) represents the gap between the dispensing nozzle and the interfacial layer.

properties, making the encapsulated system more adaptable to dynamic and complex environments. For example, the liquid medium can facilitate the movement, deformation, or reconfiguration of the encapsulated structure under external stimuli, such as magnetic fields, enabling innovative applications in responsive systems, soft robotics, and tissue engineering. Thus, liquid encapsulation combines stability, functionality, and adaptability, providing a robust approach to developing advanced materials and systems in various fields.

Building on our previous work in liquid–liquid encapsulation,[25,39–42] here we have encapsulated magnetic and non-magnetic hydrogels in a liquid phase (oil). Using a suspension droplet generation method (Fig. 1(a)), we prepare magnetic and non-magnetic hydrogels and suspend them in laser oil. We then prepare compound core droplets by allowing the mixture containing the hydrogels in oil to be dispensed from a nozzle, producing well-defined droplets. This is followed by impacting such

compound core droplets onto a liquid (canola oil) interfacial layer (shell) floating on a water bath (shown in Fig. 1(b)), creating magneto-responsive compound encapsulated cargos. We further exploit the unique magnetic properties of these encapsulated cargos, such as a magnet-assisted release of only the magnetic hydrogel of the compound encapsulated cargo inside the water bath. We demonstrate various cases of underwater magnet-assisted coalescence based on the underwater magnet-assisted manipulation of magnetic cargos. This study opens new avenues for applying magnetic hydrogels in dynamic and responsive systems.

2. Experimental

2.1 Materials and methods

2.1.1 Preparation of magnetic and non-magnetic hydrogel. First, a solution (4% w/w) of calcium chloride (CaCl$_2$) is

prepared by dissolving 1 g of the calcium chloride anhydrous powder (Sigma Aldrich, 98%) in 25 mL of deionized water. The resulting calcium chloride ($CaCl_2$) solution is divided into two parts. In one of the solutions, 200 μL polyethylene glycol (PEG) based ferrofluid (PBG 900, Ferrotec, USA) with magnetic nanoparticle concentration (17.7%), density $\rho = 1860$ kg m^{-3} is mixed to obtain a magneto-responsive solution. The other part of the solution is dyed with a commercially available orange dye (Bright Dyes FLT Orange Liquid, Product number: 106006, Kingscote CHEMICALS, USA) to obtain a coloured $CaCl_2$ solution. We used 100 μL of orange dye in the non-magnetic hydrogel solely for visualization, not based on any specific rationale. Unlike the magnetic hydrogel, which visibly diffuses upon release due to its water-miscible ferrofluid, the non-magnetic hydrogel's release was not demonstrated. Instead, the dye served as a visual indicator to confirm that the non-magnetic hydrogel remained within the encapsulated cargo (a laser oil drop wrapped in canola oil), as its diffusion would indicate release. Then, a solution (2% w/w) of sodium alginate (Sigma Aldrich, 98%, NaAlg) is prepared by dissolving 0.5 g of NaAlg powder inside 25 mL of deionized water. The selection of sodium alginate and calcium chloride concentrations in our study is based on existing literature[43,44] to achieve a stronger hydrogel membrane. Magnetic hydrogels are fabricated based on the suspension droplet generation technique.[43,44] Using the natural sedimentation method, suspension droplets of magneto-responsive calcium chloride ($CaCl_2$) solution were produced using a syringe-needle arrangement, as shown in Fig. 1(a). Magnetic hydrogels are fabricated by adding these droplets to the sodium alginate solution and allowing the suspension droplets to stay in the sodium alginate solution for one hour for the gelation process to complete. After gelation, these magnetic hydrogels are taken from the sodium alginate solution and allowed to dry in ambient air for 30 min. Incorporating the PEG-based ferrofluid into the $CaCl_2$ solution plays a significant role in this study. It enables the efficient magnetic actuation of the magnet-responsive cargo inside the water bath. The concentration of the PEG-based ferrofluid inside the $CaCl_2$ solution can control the magnetic maneuverability of the encapsulated cargo. For the fabrication of the non-magnetic hydrogels, droplets of coloured calcium chloride ($CaCl_2$) solution were produced using a syringe-needle arrangement, as shown in Fig. 1(a). These droplets are added to the sodium alginate solution, allowing the suspension droplets to stay in the sodium alginate solution for one hour for the gelation process to complete, as shown in Fig. 1(a), to form the non-magnetic hydrogels. After gelation, these non-magnetic hydrogels are taken from the sodium alginate solution and allowed to dry in ambient air for 30 min. Throughout the study, the size of the magnetic and non-magnetic hydrogels are varied by varying the needle diameter in the range of 0.52 mm to 1.83 mm, resulting in the hydrogels' size variation from $R_d = 0.050$ mm to $R_d = 1.40$ mm, where R_d is the radius of the hydrogel. The rheological characterization for the magnetic and non-magnetic hydrogel is described in Section S2, ESI.† The framework involves the encapsulation of magnetic and non-magnetic hydrogels as the core inside the liquids (oils) as the shell layer. Thus, the cores and the shell layers involved in the encapsulation process are named in a

particular manner, as shown in Fig. 1(b). Following the drying process, the hydrogels are suspended inside a laser oil bath, as shown in Fig. 1(a). The semi-solid magnetic hydrogel and the non-magnetic hydrogel inside the compound droplet (shown in Fig. 1(b)) are called the inner magnetic core ($S_{ic,m}$) and the inner non-magnetic core ($S_{ic,nm}$), respectively. Throughout this study, "S" indicates the semi-solid hydrogel, subscripts "ic," "m" and "nm" indicates the inner core, the magnetic and non-magnetic. The density of the dried magnetic and non-magnetic hydrogels are $\rho_{ic,m} = 1136$ kg m^{-3} and $\rho_{ic,nm} = 1051$ kg m^{-3}, respectively. The outer core liquid in the compound droplet is called the outer core liquid (L_{oc}). Throughout this study, "L" indicates the liquid involved in the encapsulation process, and subscript "oc" indicates the outer core. Throughout the study, the outer core liquid (L_{oc}) in the compound droplet (shown in Fig. 1(b)) is kept fixed, a class of laser liquid – a mixture of silicanes and polyphenol ethers with a water solubility of <0.1% (Product Code: 57B63, Cargille Laboratories Inc., Cedar Grove, NJ, USA). The relevant material properties are as follows: density $\rho_{oc} = 1900$ kg m^{-3}, dynamic viscosity $\mu_{oc} = 1024$ mPa s, liquid–air surface tension $\gamma_{oc} = 50$ mN m^{-1}, and liquid–water interfacial tension $\gamma_{oc-h} = 39.4$ mN m^{-1}. The liquid–water interfacial tension and liquid–air surface tension were measured using pendant drop tensiometry. The liquid L_h, where the subscript "h" indicates the host that is chosen to be deionized (DI) water (purified by Milli-Q, MilliporeSigma, Ontario, Canada) with density $\rho_h = 1000$ kg m^{-3} and dynamic viscosity $\mu_h = 1$ mPas, liquid–air surface tension $\gamma_h = 72$ mN m^{-3}. The liquid that floats on the host bath is termed the interfacial layer liquid L_{os}, the outermost shell layer, where the subscript "os" indicates the outermost shell, as shown in Fig. 1(b). Throughout the study, the interfacial liquid layer (L_{os}) floating on the host water bath comprises canola oil (manufactured and marketed under Clic International Inc., Ottawa, Canada) with density $\rho_{os} = 913$ kg m^{-3}, dynamic viscosity $\mu_{os} = 63.5$ mPa s, and canola oil–air surface tension $\gamma_{so} = 31.03$ mN m^{-1}, canola oil–water interfacial tension $\gamma_{so-h} = 18.01$ mN m^{-1} and canola oil–laser oil interfacial tension $\gamma_{oc-os} = 2.22$ mN m^{-1}. The canola oil–water interfacial tension was measured using pendant drop tensiometry. The canola oil–laser oil interfacial tension is calculated using the interfacial formula for non-polar liquids as $\gamma_{oc-os} = \gamma_{oc} + \gamma_{os} - 2\sqrt{\gamma_{oc}\gamma_{os}}$. The density and viscosity values for each liquid are taken from the manufacturer's datasheet.

Before each experiment, the glass cuvette containing the host water bath was thoroughly cleaned. It was first soaked and ultrasonicated (Branson 5800, Emerson Electric Co., USA) in hexane for 30 min. Afterward, it was rinsed thoroughly with deionized (DI) water and acetone and dried using compressed nitrogen. To ensure uniform wettability along the cuvette walls and consistent spreading of the interfacial liquid layer, the cuvette was treated with air plasma for 10 min (PE-25, PLASMA ETCH, USA), as described in our previous study.[45] The cleaned cuvette was mounted on a vertically adjustable stage (Kruss GmbH, Hamburg, Germany) and partially filled with 90 mL of DI water, serving as the host liquid bath. A specific volume of the interfacial liquid was carefully dispensed onto the host bath using a pipette (DiaPETTE, Canada). The liquid spread uniformly within ∼2 min, forming a thin interfacial layer

of controlled thickness. The compound droplet dispenser was then positioned at a fixed height $H = 7$ cm using a linear translating stage to ensure precise droplet impact. Fig. 1(b) shows the impact of a compound droplet of magnetic and non-magnetic hydrogels inside the laser oil on the interfacial layer. Here, hydrogel-laser oil suspension was pushed through the vertically oriented microtip (inner diameter of 4 mm) attached to a syringe. Upon detachment from the microtip, the compound droplet accelerates downward due to gravity and encounters the interfacial layer. The compound drop overcomes the interfacial and viscous barriers and penetrates through the interfacial layer due to sufficient kinetic energy. This process results in the wrapping of the compound drop by the interfacial layer. Typically completed in ~ 200 ms, the encapsulation process was recorded using a high-speed camera (Photron FAS-TCAM Mini AX200) at 6400 frames per second. The camera, paired with a Navitar 7000 Zoom lens (focal length: 18–108 mm), captured the dynamics in high resolution (1024 × 1024 px). With 32GB of internal memory, the camera provided a recording window of ~ 3.41 s, sufficient for capturing the complete process. Using the "end" trigger mode, the recording began after visually confirming the completion of encapsulation, ensuring all prior interface dynamics were captured. The recorded data was transferred to a computer *via* a high-speed Ethernet connection for further analysis. Additionally, colour images were taken with a DSLR camera (Nikon D5200) for improved visualization.

3. Results and discussion

3.1 Underlying mechanism involved in the encapsulation of magnetic and non-magnetic hydrogel

Fig. 2 presents a detailed step-by-step visualization of the high-speed interface dynamics that encapsulate a compound core droplet containing magnetic and non-magnetic hydrogel. The encapsulation of the compound droplet is governed by a complex interplay between several forces, including interfacial

(surface) tension forces, viscous forces, and momentum at the interface of four distinct fluids: air, the interfacial layer, the host liquid, and the outer core. The encapsulation process begins with releasing the compound core droplet, dispensed from a needle positioned at a vertical height $H = 7$ cm above the interfacial layer. This vertical separation imparts sufficient kinetic energy to the droplet as it falls toward the interfacial layer. To quantify the impact kinetic energy of the compound droplet, we have used the impact Weber number We_i. The impact Weber number is defined as

$$We_i = \left[\beta_{ic,m} \rho_{ic,m} + \beta_{ic,nm} \rho_{ic,nm} + \left(1 - \beta_{ic,m} - \beta_{ic,nm}\right) \rho_{oc} \right] \frac{D_c V^2}{\gamma_{oc}},$$

where $\beta_{ic,m}$ and $\beta_{ic,nm}$ are the volume fractions of the magnetic and non-magnetic inner core in the compound droplet, $\rho_{ic,m}$, $\rho_{ic,nm}$ and ρ_{oc} are the densities of the inner magnetic core, inner non-magnetic core and outer core, respectively. D_c and γ_{oc} are the diameter of the compound drop and the surface tension of the outer core liquid (laser oil). V is the impact velocity of the compound droplet, estimated as $V = \sqrt{2gH}$, where g is the acceleration due to gravity, H is the impact height. For $H = 7$ cm, $\beta_{ic,m} = 0.0385$, $\rho_{ic,m} = 1136$ kg m^{-3}, $\rho_{ic,nm} = 1051$ kg m^{-3}, $\rho_{oc} = 1900$ kg m^{-3}, $D_c = 3.48$ mm and $\gamma_{oc} = 52$ mN m^{-1}, we get $We_i = 175$. Upon reaching the interfacial layer L_{os}, the droplet encounters resistance due to interfacial tension and viscous forces. At $t = 0.0$ ms, the compound droplet impacts the interfacial layer. Upon contact, the droplet attempts to penetrate the layer, dragging it downward due to the momentum acquired during its fall. This downward motion deforms the interface between the interfacial layer L_{os} and the host liquid L_h, causing a significant increase in the surface area of the interface. However, interfacial tension forces act to restore the deformed interface to its original position, aiming to minimize interfacial energy. Simultaneously, the interfacial layer offers viscous resistance, dissipating the droplet's momentum and further opposing its downward motion. As a result of this competition between the droplet's momentum and the resisting forces, a necking process begins to form in the interfacial layer. This process, visible in Fig. 2, continues over several milliseconds. By $t = 4.2$ ms, the droplet has sufficiently deformed the interfacial layer, initiating further
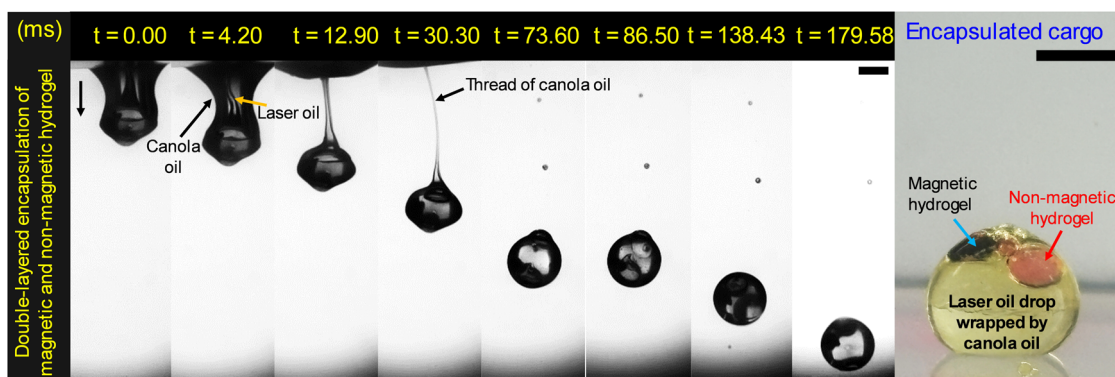

Fig. 2 Time-resolved high-speed image sequence of double-layered encapsulation showing the interface evolution during the impact-driven wrapping of magnetic and non-magnetic hydrogels-laser oil compound core droplet by canola oil interfacial layer. The various steps of the encapsulation process are represented, and the liquids involved are identified with different colours. The motion of the droplet is indicated using a black arrow. The laser oil, magnetic and non-magnetic hydrogels are identified using yellow, blue and red arrows, respectively. The impact Weber number associated with the encapsulation process is $We_i = 175$ (achieved using $H = 7$ cm). The rightmost colour image depicts the final settled wrapped cargo. The time is in milliseconds (ms), and the scale bar in each image represents 2 mm.

downward penetration. The necking process becomes more pronounced as the droplet progresses, driven by its kinetic energy, overcoming the resistance of interfacial tension and viscous forces. At t = 12.9 ms, the thinning of the neck in the interfacial layer becomes evident as the liquid threads of the canola oil begin to elongate. This process continues until t = 30.3 ms, during which the droplet continues its descent through the host liquid toward the bottom of the cuvette. At this stage, the neck thins beyond a critical point, and at t = 73.6 ms, the encapsulated droplet detaches from the interfacial layer. This detachment forms a thin encapsulating shell of canola oil around the compound droplet. The encapsulated hydrogels, now enclosed within a double-layered shell of laser oil and canola oil, continue settling at the bottom of the cuvette. By t = 179.58 ms, the encapsulation process is complete, and the compound droplet is fully stabilized. Throughout this encapsulation process, the integrity of the inner core, consisting of magnetic and non-magnetic hydrogels, remains intact. This stability is illustrated in Fig. 2, where blue and red arrows indicate the magnetic and non-magnetic hydrogels, respectively. The final image in Fig. 2 shows the fully encapsulated compound droplet, comprising the magnetic and non-magnetic hydrogels securely wrapped within two protective layers: laser oil and canola oil. This stepwise encapsulation process demonstrates the intricate dynamics of creating stable, multi-layered encapsulated systems, offering insights into the interplay of forces at different fluid interfaces. Such systems have potential applications in advanced material design, drug delivery, and responsive systems.

3.2 Thermodynamic criteria for successful encapsulation

In our previous studies,[25,39–42] we successfully encapsulated a single core droplet using an interfacial layer floating on a host water bath. Those investigations established the thermodynamic criterion for forming a stable encapsulated droplet. In those experiments, laser oil served as the core droplet, while canola oil acted as the interfacial shell layer atop the host water bath. The thermodynamic criterion derived from those studies can be extended to the present system by appropriately substituting the interfacial tension values of the fluids involved. The criterion is represented as follows:

$$\gamma_{\text{oc-h}} - \gamma_{\text{oc-os}} - \gamma_{\text{os-h}} > 0 \qquad (1)$$

where, $\gamma_{\text{oc-h}}$ is the interfacial tension between the outer core (laser oil) and host water bath, $\gamma_{\text{oc-os}}$ is the interfacial tension between the outer core (laser oil) and outer shell (canola oil), and $\gamma_{\text{os-h}}$ is the interfacial tension between the outer shell (canola oil) and host water bath. This equation is based on the principle of minimizing interfacial energy before and after the impact and is governed solely by the surface and interfacial tensions of the system. Notably, the surface or interfacial energy of the inner magnetic core ($S_{\text{ic,m}}$) and the inner non-magnetic core ($S_{\text{ic,nm}}$) is not important in determining the thermodynamic feasibility of the impact-driven encapsulation of the compound droplet. Since the inner magnetic and non-magnetic core is already enclosed by the outer core liquid (L_{oc}, here laser oil) in the compound droplet, it does not directly participate in the interfacial interactions with the shell liquid L_{os} or the host bath L_{h}. Instead, the interfacial energy of the

outer core is critical in assessing the overall energetic favorability of forming the final encapsulated droplet. Substituting the experimentally measured interfacial tension values for our liquid system into eqn (1), we find that for our combination involving laser oil (outer core), canola oil (outer shell), and water (host liquid), yields ($\gamma_{\text{oc-h}} - \gamma_{\text{oc-os}} - \gamma_{\text{os-h}}$ = 39.4 − 2.22 − 18.01) mN m^{-1} = 19.17 mN m^{-1} > 0. This estimation demonstrates that the thermodynamic criterion is satisfied, confirming the energetic favorability of encapsulating a compound droplet consisting of the magnetic and non-magnetic hydrogel as the inner core, laser oil as the core, canola oil as the shell, and water as the host liquid. The choice of laser oil as the inner core and canola oil as the outer shell for encapsulating magnetic and non-magnetic hydrogels is based on fundamental thermodynamic principles. However, our previous studies on impact-driven liquid–liquid encapsulation have shown that various oils, such as silicone oil, mineral oil, oil-based ferrofluid, and PDMS,[25,40,42,45] can also serve as the outer shell layer (equivalent to canola oil in this study). In all cases, the thermodynamic criteria for successful encapsulation are met. Experimental images corroborate these findings, showing that the compound droplet remains stably encapsulated within the canola oil shell. Experimental high-speed imaging (Fig. 2) also provides further evidence of stability during encapsulation. For instance, the inner magnetic core (in Fig. 2, t = 73.60 ms and t = 86.50 ms) and inner non-magnetic core (in Fig. 2, t = 73.60 ms and t = 86.50 ms) maintain their structural integrity throughout the interfacial evolution. Even after encapsulation, the inner magnetic and non-magnetic cores remain stable and fully encapsulated within the host water bath, further validating the reliability of the encapsulation mechanism for both static and dynamic systems.

3.3 Mechanism of extraction of the magnetic hydrogel from the encapsulated cargo

In this section, we discuss the mechanism of extracting a magnetic hydrogel from the encapsulated cargo using a static magnetic field produced by the presence of a permanent magnet fixed at an offset below the cuvette holding the encapsulated cargo. Fig. 3(a)–(e) shows the schematic of the experimental setup and the process of the magnet-assisted extraction of the encapsulated cargo. After the encapsulation process, described in Section 3.1, cargo containing the magnetic and non-magnetic hydrogels settle at the bottom of the cuvette. The magnet-assisted extraction of the magnetic hydrogel is achieved using a cubic neodymium (NdFeB) permanent magnet of size 12.7 mm (N52, remnant flux density B_{r} = 1.48 T, K&J Magnetics Inc. USA) placed at an offset (l_1) to the axis of the encapsulated cargo and positioned beneath the cuvette at a distance (h) from the cuvette bottom. The magnetic field was estimated using a 3D numerical simulation carried out in the computational framework of COMSOL Multiphysics. The variation of the magnetic field and the details of the COMSOL simulation are provided in Section S1, ESI.†

The extraction of magnetic hydrogel from the encapsulated cargo is explained in five stages (Fig. 3(a)–(e)). Fig. 3(a)–(e)

contains the schematic representation of the experimental setup and the corresponding stage of the extraction process. Once the droplet settles at the cuvette bottom (Fig. 3(a)), a separation exists between the axis of the encapsulated cargo and the magnetization axis of the magnet, denoted as l_1. Owing to the offset l_1, the magnetic nanoparticles (MNPs) inside the magnetic hydrogel experience a magnetic force[46] ($F_m \sim \mu_0 \chi R_d^3 \nabla H^2$). In this case, the magnetic hydrogel migrates toward the axis of magnetization. Thus, the magnetic force results in the migration of the magnetic hydrogel from its initial position toward the laser oil–canola oil interface, as shown in Fig. 3(b). During this migration of the magnetic hydrogel inside the laser oil, the encapsulated cargo remains almost at the same location. The relocation of the magnetic hydrogel inside the encapsulated cargo toward the interface near the axis of magnetization happens almost instantaneously. Therefore, no significant change is observed in the

separation (l_1) between the axis of the cargo and the axis of the magnet's magnetization (Fig. 3(b)). However, the reduction in the gap between the magnetic hydrogel and the magnet enhanced the magnetic interaction between the magnetic hydrogel and the magnet. Owing to this enhancement of magnetic interaction, the x-component ($F_{m,x}$) of the magnetic force acting on the hydrogel results in the motion of the encapsulated cargo toward the magnet. Once the cargo starts its linear translation towards the cargo, it experiences a viscous drag ($F_d = -6\pi\mu_h R_c v_c$) offered by the surrounding water opposing the motion of the cargo. Here, μ_h is the viscosity of the host water, R_c is the radius of the cargo and v_c is the speed of the cargo. The interplay between the magnetic force and the viscous drag governs the migration of the encapsulated cargo. As a result of this migration, the gap between the axis of the cargo and the axis of the magnet's magnetization was reduced from l_1 to l_2, as shown in Fig. 3(c). As a result of this reduction,
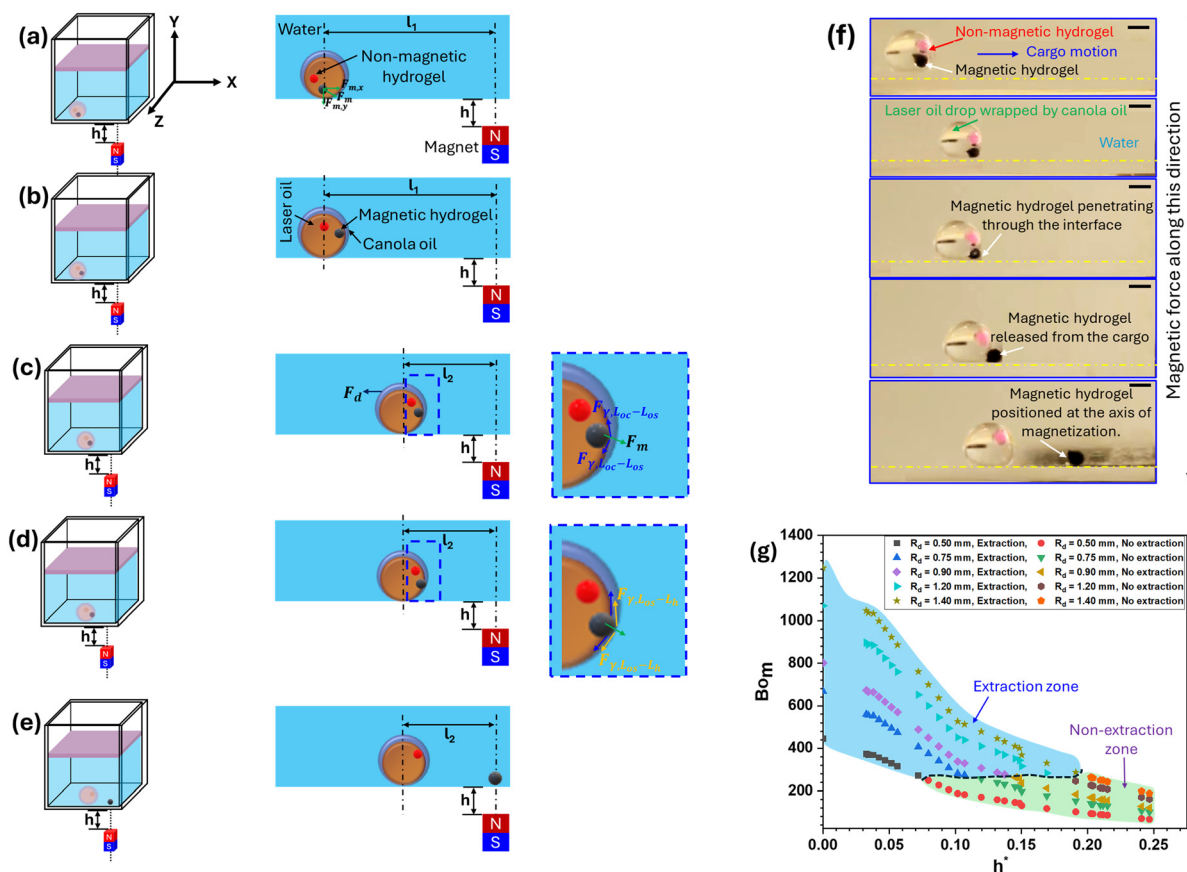

Fig. 3 (a)–(e) Schematic representation of the extraction of the magnetic hydrogel from the encapsulated cargo consisting of the magnetic and non-magnetic hydrogels as the inner core, laser oil as the outer core and canola oil as the outer shell inside a host water bath. The magnet is kept beneath the cuvette bottom at a gap of h. The left panel images in (a)–(e) show the location of the encapsulated cargo inside the host water bath before and after the release of the magnetic hydrogel from the cargo. The middle panel images in (a)–(e) depict the zoomed view of the encapsulated cargo corresponding to the images in the left panel of (a)–(e). The middle panel images also depict the magnetic force (F_m) acting on the magnetic hydrogel and the viscous drag (F_d) offered by the host water bath on the cargo. The right panel images in (c), (d) depict the zoomed view (blue dotted box) of the corresponding middle panel images (c)–(e), where the interfacial forces acting at the interface of the laser oil–canola oil ($F_{\gamma, L_{oc}-L_{os}}$) and canola oil–water interface ($F_{\gamma, L_{os}-L_h}$) are shown. (f) Experimental time-lapse images depict the magnetic hydrogel extraction from the encapsulated cargo. The yellow dotted line represents the cuvette bottom. The scale bar represents 2 mm. (g) The plot demonstrates the regime map showing the extraction and non-extraction zones of the magnetic hydrogel from the encapsulated cargo. The characterization depicts the dependence of the magnetic Bond number (Bo$_m$), the non-dimensional gap (h^*) between the magnet and the cuvette bottom and the radius of the magnetic hydrogel (R_d).

the magnetic hydrogel comes closer to the magnet (*i.e.*, towards the liquid–liquid interfaces), further enhancing the magnetic interaction between the MNPs inside the magnetic hydrogel and the magnet. At this stage, the magnetic hydrogel encounters two interfaces, first between the laser oil–canola oil and second between the canola oil–water interface, offering the interfacial forces $F_{\gamma,L_{oc}-L_{os}}$ and $F_{\gamma,L_{os}-L_h}$, respectively. The interfacial forces[47] scale as $F_{\gamma,L_{oc}-L_{os}} \sim R_d \gamma_{oc\text{-}os}$ at the laser oil–canola oil interface and $F_{\gamma,L_{os}-L_h} \sim R_d \gamma_{os\text{-}h}$ at the canola oil–water interface, where R_d is the radius of the hydrogel. The interface between the laser oil and canola oil and the interface between the canola oil and water tries to resist the deformation caused by the magnetic hydrogel. On the contrary, the hydrogel tries to penetrate through the interface to attain the zone of maximum magnetic field (Fig. 3(d)). If the magnetic force is strong enough to overcome the combined interfacial tension offered by the laser oil–canola oil and canola oil–water, the magnetic hydrogel penetrates through the interfaces and attains the zone of the highest magnetic field, as shown in Fig. 3(e). In this case, $\boldsymbol{F}_m \sim$ 19.6 µN. Here, $\mu_0 = 4\pi \times 10^{-7}$ H m^{-1}, permeability of free space, $\chi \approx 2$, magnetic susceptibility of the magnetic nanoparticles inside the magnetic hydrogel, R_d is the radius of the magnetic hydrogel, H is the magnetic field. The order of the magnetic force is estimated based on the smallest hydrogel $R_d = 0.050$ mm. In this case $F_{\gamma,L_{oc}-L_{os}} \sim 1.11$ µN and $F_{\gamma,L_{os}-L_h} \sim 9$ µN. The order of the interfacial forces is estimated based on the smallest hydrogel $R_d = 0.050$ mm.

Fig. 3(f) depicts an experimental time-lapse image demonstrating the extraction of magnetic hydrogel from the encapsulated cargo and attaining the axis of magnetization (zone of highest magnetic field). The direction of the cargo motion and the direction of magnetic force are indicated with blue and black arrows in Fig. 3(f). The yellow dotted line in Fig. 3(f) represents the cuvette bottom. It can be observed that the encapsulated cargo migrates toward the direction of the highest magnetic field due to the magnetic interaction between the magnetic hydrogel and the magnetic field. The magnetic hydrogel tries to penetrate through the laser oil–canola oil interface and canola oil–water interface and gets released from the encapsulated cargo. Once released, the magnetic hydrogel attains the position of the maximum magnetic field and aligns itself along the direction of the magnetization of the magnetic field, as shown in Fig. 3(f).

To understand the effects of various experimental parameters, we have performed a large set of experiments and characterized the behaviour of the magnetic hydrogel extraction, as shown in Fig. 3(g). The characterization is depicted in terms of two non-dimensional parameters, *viz.*, the magnetic Bond number (Bo$_m$) and the gap ($h^\star$). The magnetic Bond number (Bo$_m$) represents the ratio of the magnetic force to the combined interfacial tension force offered by the laser oil–canola oil and canola oil–water interfaces. The magnetic Bond number, defined as $\mathrm{Bo}_m = \dfrac{\mu_0 H^2 R_d}{\gamma_{oc\text{-}os} + \gamma_{os\text{-}h}}$,[48] which is the ratio of magnetic force and interfacial tension force. Here $\mu_0 = 4\pi \times 10^{-7}$ H m^{-1} is the magnetic permeability of free space, H is the

magnitude of the applied H-field (A m^{-1}), R_d is radius of the magnetic hydrogel. The non-dimensionalized gap ($h^\star$) is estimated by dividing the gap (h) between the magnet and the cuvette bottom by the magnet dimension (cubic magnet of size 12.7 mm). In our experiments, the separation (l_1) between the axis of the encapsulated cargo and the axis of magnetization of the magnet is kept fixed in each case. This is done by keeping the initial location of the encapsulated cargo and the magnet fixed. Since the magnetic Bond number (Bo$_m$) represents the ratio of the magnetic force to the combined interfacial tension force offered by the interfaces, the variation in Bo$_m$ can be achieved by the variation in the magnetic force or the force due to interfacial tension. The magnetic force can be varied by varying the size of the magnetic hydrogel or the magnetic field. In our experiments, the size of the magnetic hydrogel is varied between $R_d = 0.5$ mm to $R_d = 1.4$ mm (as mentioned in Section 2) and the non-dimensionalized gap between the magnet and the cuvette bottom is varied between $h^\star = 0.00$ to $h^\star = 0.24$. From Fig. 3(f), it can be inferred that a particular $h^\star$, the increase in the Bo$_m$ is achieved by increasing the radius of the magnetic hydrogel R_d. An increase in the radius of the magnetic hydrogel results in an increase in the magnetic force ($\boldsymbol{F}_m \propto R_d^3 \nabla H^2$). The key inference from the regime plot presented in Fig. 3(f) is that with an increase in the size of magnetic hydrogel (R_d), the zone of extraction is extended to a higher $h^\star$, *i.e.*, extraction could be achieved even for a larger vertical distance between the cuvette bottom and the magnet. The cubic dependency of the magnetic force on the size of the hydrogel can overcompensate the reduction in magnetic force due to an increment in $h^\star$, thereby ensuring successful extraction even when the magnet is placed further away.

3.4 Underwater manipulation of the hydrogel-encapsulated cargo

This section presents underwater manipulations involving magneto-responsive encapsulated cargo to highlight their versatility and potential applications. Specifically, we illustrate two situations: first, the coalescence occurs between an encapsulated magnetic cargo (containing magnetic hydrogel) and an encapsulated core drop (*i.e.*, without any hydrogel), and second, the coalescence occurs between an encapsulated magnetic cargo (containing magnetic hydrogel) and a non-magnetic cargo (containing non-magnetic hydrogel). As discussed in the materials and methods (Section 2), magnetic and non-magnetic hydrogels (inner core) are first enclosed inside a carrier medium of laser oil before executing the impact-driven wrapping process of the compound droplet by the canola oil interfacial layer liquid. The laser oil carrier phase plays an important role here. The canola oil-wrapped compound droplet essentially has a double-layered morphology. The inner hydrogel core is surrounded by two shell layers: a laser oil shell in direct contact with the hydrogel (magnetic or non-magnetic) and the outer canola oil layer. The intermediate viscous laser oil provides an additional diffusion barrier that prevents unwanted interaction of the hydrogel (magnetic or non-magnetic) with the surrounding water bath. It improves the
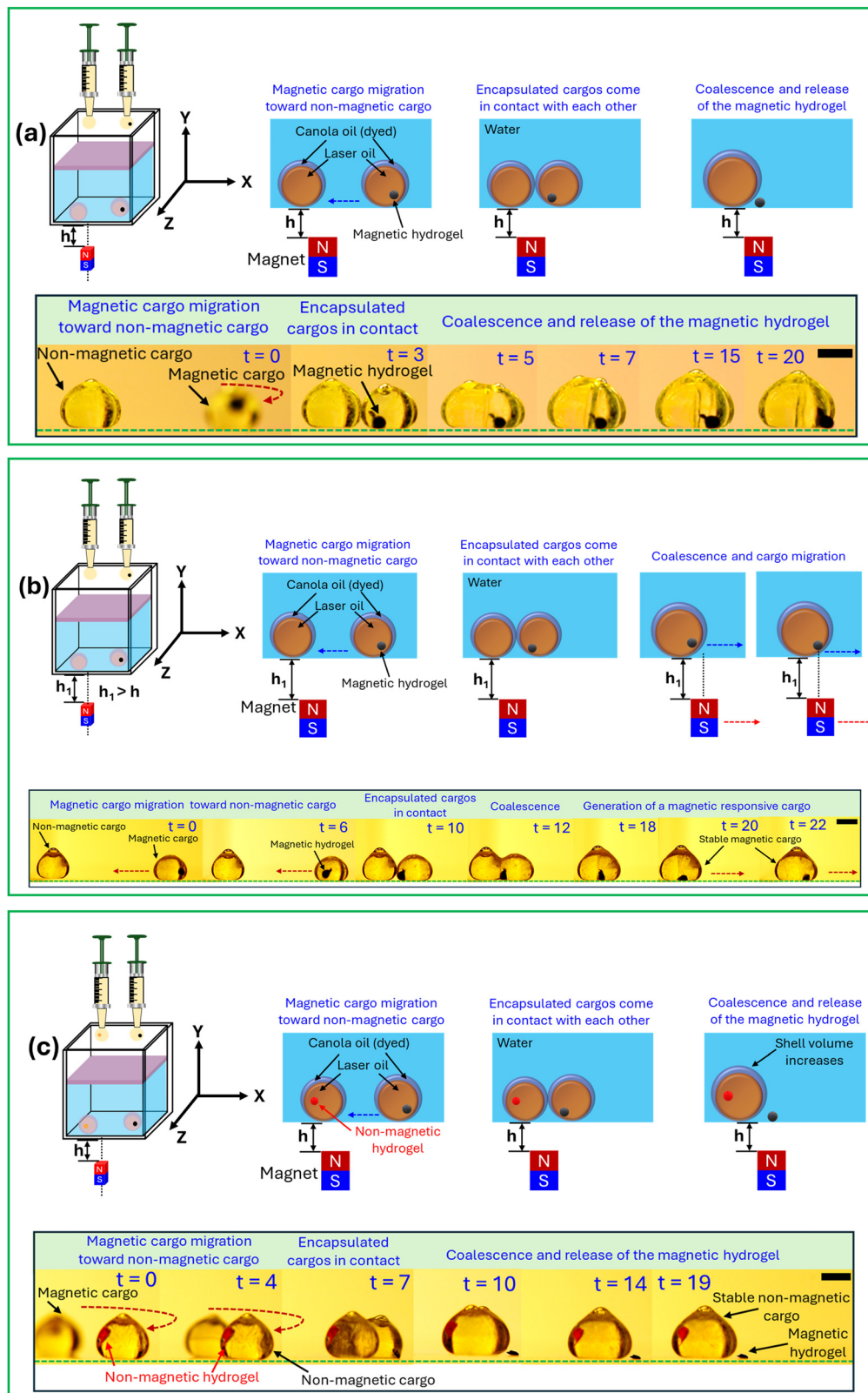
Fig. 4 (a) Schematic representation depicting the coalescence of the encapsulated magnetic cargo (containing magnetic hydrogel) and encapsulated core drop (without any hydrogel) followed by the release of the magnetic hydrogel. The magnet is placed beneath the cuvette at a gap (h). The impact Weber numbers (We_i) for the non-magnetic and magnetic cargo are $We_i = 181$ and $We_i = 178$, respectively. The experimental time-lapse image depicts the coalescence process where the gap between the magnet and the cuvette bottom is $h^* = 0.05$, which corresponds to the magnetic Bond number ($Bo_m = 385$). The red-dotted curved line in experimental time-lapse images indicates the direction of migration of the magnetic cargo. (b) Schematic representation depicting the coalescence of the encapsulated magnetic cargo (containing magnetic hydrogel) and encapsulated core drop (without any
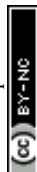
hydrogel) followed by the non-release of the magnetic hydrogel. The magnet is placed beneath the cuvette at a gap (h_1). The impact Weber numbers (We_i) for the non-magnetic and magnetic cargo are $We_i = 181$ and $We_i = 178$, respectively. The experimental time-lapse image depicts the coalescence process where the gap between the magnet and the cuvette bottom is $h^* = 0.15$, which corresponds to the magnetic Bond number ($Bo_m = 80$). The red-dotted line in experimental time-lapse images indicates the direction of migration of the magnetic cargo. In this experiment, at $t = 20$ s and $t = 22$ s, the encapsulated cargo migrates with the motion of the magnet. The sole purpose of this demonstration is to show that by reducing the magnetic field, we can restrict the extraction of the magnetic hydrogel from the final encapsulated cargo and transport the cargo using a moving magnetic field. (c) Schematic representation depicting the coalescence of the encapsulated magnetic cargo (containing magnetic hydrogel) and non-magnetic cargo (containing non-magnetic hydrogel), followed by the preferential release of the magnetic hydrogel. The magnet is placed beneath the cuvette at a gap (h). The impact Weber numbers (We_i) for the non-magnetic and magnetic cargo are $We_i = 178$. The experimental time-lapse image depicts the coalescence process where the gap between the magnet and the cuvette bottom is $h^* = 0.05$, which corresponds to the magnetic Bond number ($Bo_m = 385$). The red-dotted curved line in experimental time-lapse images indicates the direction of migration of the magnetic cargo. The scale bar represents 2 mm. The volume of the interfacial layer (canola oil) used in these experiments is 400 μL. The blue dotted line in each schematic indicates the direction of motion of the magnetic cargo toward the non-magnetic cargo. The green dotted line in each case represents the cuvette surface (bottom).

controllability of the manipulation and subsequent coalescence of the encapsulated cargo and aids in the robustness of the developed platform.

Fig. 4 shows the experimental schemes and time-lapse experimental images demonstrating three cases of underwater magnet-assisted coalescence: (a) controlled release of the magnetic hydrogel when an encapsulated core drop is in contact with the encapsulated magnetic hydrogel, (b) arrest of the release of the magnetic hydrogel when an encapsulated core drop is in contact with the encapsulated magnetic hydrogel and (c) preferential release of the magnetic hydrogel when an encapsulated magnetic hydrogel is in contact with encapsulated non-magnetic hydrogel. Let us first understand the underwater magnet-assisted coalescence of an encapsulated core drop and a magnetic cargo (containing magnetic hydrogel). The encapsulated core drop is generated by impacting a laser oil droplet on a canola oil interfacial layer floating on the host water bath, as described in one of our previous studies[41] and shown in Fig. 4(a). The magnetic cargo containing the magnetic hydrogel is generated by impacting a compound droplet containing a magnetic hydrogel wrapped by laser oil onto the canola oil interfacial layer floating on the host water bath, as shown in Fig. 4(a). The schematic of the experimental setup is shown in Fig. 4(a). Here, the permanent magnet is kept fixed beneath the cuvette bottom at a gap (h), closer to the encapsulated laser oil drop. The schematic and the time-lapse image sequence depict the controlled coalescence process of an encapsulated core drop and a magnetic cargo (containing magnetic hydrogel). The controlled coalescence process can be described in three steps: (i) owing to the magnetic interaction between the magnetic field and the magnetic hydrogel, the magnetic hydrogel migrates inside the double-layered encapsulated cargo (toward the axis of magnetization). The magnetic force results in the migration of the magnetic hydrogel from its initial position toward the laser oil–canola oil interface and the motion of the encapsulated magnetic cargo toward the magnet (eventually drawing it closer to the encapsulated core drop), as described in Section 3.3 and shown in Fig. 4(a) (blue dotted arrow). (ii) The two encapsulated cargos come in contact due to this motion. The magnetic hydrogel is closer to the magnet at this instant and experiences a much stronger magnetic force than the previous instant (i). Due to

this strong magnetic force, the magnetic cargo tries to push the encapsulated core drop toward the negative x-axis (i.e., along its direction of motion) to occupy the zone of the maximum magnetic field (see Supporting Movie 1, ESI†). During this cargo–cargo interaction, the thin film of canola oil wrapping the individual cargos at the point of contact drains, and film thinning begins. (iii) As the film thickness reduces due to film drainage, the van der Waals force comes into play, resulting in the rupture of the thin canola oil film and the merging of the two encapsulated cargos (see Supporting Movie 1, ESI†).

The time-lapse image shown in Fig. 4(a) depicts the experimental observations depicted above. Due to the magnetic force experienced by the magnetic hydrogel, the magnetic cargo migrates toward the non-magnetic (encapsulated laser oil) empty cargo ($t = 0$ s), and the cargos come into contact with each other ($t = 3$ s). At $t = 5$ s, coalescence begins, and the two cargos merge, forming a larger cargo, which is now encapsulated by the canola oil. Since the magnetic Bond number ($Bo_m = 385$) in this experiment corresponds to the region where the extraction of the magnetic hydrogel is observed (Section 3.3); we observe the eventual release of the magnetic cargo ($t = 20$ s) (Supporting Movie 1, ESI†). It should be noted that the demonstrated underwater magnet-assisted manipulation of the magnetic hydrogel facilitates an overall increase in the volume of the laser oil (outer core) and the canola oil (outer shell) due to the merging of the two encapsulated cargos. However, in this case, magnet-assisted coalescence results in an overall encapsulated cargo without any magnetic load due to the release of the magnetic hydrogel.

To further demonstrate the potential of underwater magnet-assisted coalescence, we have demonstrated that by reducing the magnetic field, we can restrict the extraction of the magnetic hydrogel from the merged encapsulated cargo post-coalescence. By doing so, we achieve an overall increment of the volume of the laser oil (outer core) and the canola oil (outer shell) and generate a magneto-responsive cargo (i.e., magnetic hydrogel remains inside the merged encapsulated cargo) with thicker shell volumes, as shown in Fig. 4(b). In this case, the encapsulation and magnetic manipulation process remains the same, as described in Fig. 4(a). The primary difference in this case is the gap (h_1), which is larger than the gap (h) in Fig. 4(a). The corresponding magnetic Bond number ($Bo_m = 80$) in the

case of Fig. 4(b) corresponds to the non-extraction zone of the magnetic hydrogel as described in Section 3.3. In this case, after the coalescence process, the resulting cargo contains the magnetic hydrogel, and the cargo can be transported using the moving magnet (at t = 20 s to t = 22 s), as shown in Fig. 4(b) and Supporting Movie 2 (ESI†).

Further extending the underwater magnet-assisted manipulation of the magnetic hydrogel, we demonstrate the preferential release of the magnetic hydrogel post-coalescence without the extraction of the non-magnetic hydrogel, as shown in Fig. 4(c). In this case, the encapsulated cargo containing the non-magnetic hydrogel is generated by impacting a compound droplet containing a non-magnetic hydrogel (*i.e.*, without any MNP during the synthesis process) wrapped by laser oil onto the canola oil interfacial layer floating on the host water bath, as shown in Fig. 4(c). The encapsulated magnetic cargo containing the magnetic hydrogel is generated by impacting a compound droplet containing a magnetic hydrogel wrapped by laser oil onto the canola oil interfacial layer floating on the host water bath, as shown in Fig. 4(c). The schematic of the experimental setup is shown in Fig. 4(c), where the permanent magnet is kept fixed beneath the cuvette bottom at a gap (h), shown in Fig. 4(c) (similar initial configuration to the one shown in Fig. 4(a)). At t = 0 s, the magnetic cargo begins to migrate toward the non-magnetic cargo (containing non-magnetic hydrogel). At t = 7 s, the two encapsulated cargos come in contact with each other, resulting in the coalescence and the extraction of the magnetic hydrogel at t = 10 s. It should be noted that during the complete coalescence process, the non-magnetic hydrogel remains stable inside the encapsulated cargo (t = 19 s), which is now wrapped with canola oil. The complete coalescence process remains the same as described earlier in this section and can be seen in Supporting Movie 3 (ESI†). Again, like the case in Fig. 4(a), the magnetic Bond number (Bo_m = 385) corresponds to the extraction zone of the magnetic hydrogel. Thus, we observe the extraction of the magnetic hydrogel from the resulting encapsulated cargo. More importantly, this demonstration further bolsters that despite having a non-magnetic hydrogel inside an encapsulated cargo, post coalescence, our underwater magnet-assisted manipulation can preferentially release the magnetic component into the surrounding liquid medium.

4. Conclusions

This study presents a novel impact-driven encapsulation method for creating stable, liquid-wrapped magneto-responsive hydrogels. Encapsulating magnetic and non-magnetic hydrogels within a dual liquid shell (laser oil inner layer, canola oil outer layer) in a water bath enables precise underwater manipulation for drug delivery, micro-robotics, tissue engineering, and controlled chemical synthesis applications. By leveraging magnetic responsiveness, we demonstrate controlled hydrogel release and selective extraction. The offset between the magnetization axis and the magnetic hydrogel generates a magnetic force that

pushes the magnetic hydrogel toward liquid interfaces formed by the laser oil–canola oil and canola oil–water. If the magnetic force is strong enough to overcome the combined interfacial force offered by the laser oil–canola oil and canola oil–water interfaces, the magnetic hydrogel penetrates through the liquid layers (laser oil and canola oil) and results in the extraction of the magnetic hydrogel. A key focus of this work was the characterization of the magnetic Bond number, which governs the manipulation of the encapsulated cargo and release of magnetic hydrogels under varying magnetic field conditions. These characterizations and the regime map provide valuable insights into the interplay between magnetic forces and the forces due to interfacial tensions, enabling precise control of the encapsulated cargos. Further, we exploit the magnetic maneuverability of the magneto-responsive cargos to achieve underwater magnet-assisted coalescence. We found that this technique facilitates the preferential release and arrest of the magnetic hydrogel, post coalescence, based on the strength of the applied magnetic field, which is varied by changing the distance between the magnet and the encapsulated cargos. Under a specific applied magnetic field, the magnetic hydrogel can only be released *vis-à-vis* the non-magnetic hydrogel, though both hydrogels are present inside the same encapsulated cargo, post coalescence. This research advances magnet-assisted actuation technologies, offering a stable, tunable, and adaptable platform for biomedical applications, soft robotics, and multifunctional materials. These findings pave the way for developing dynamic, responsive systems with tailored functionalities for future scientific and industrial applications.

Author contributions

U. B. performed the experiments. U. B. and S. M. analyzed the data. U. B. wrote the manuscript with inputs from all the authors. S. K. M. conceived the study and supervised the research.

Conflicts of interest

The key liquid–liquid encapsulation technology has led to a startup, SLE Enterprises B. V. and SLE Enterprises Inc. Both S. M. and S. K. M. have equity stakes in the startup.

Acknowledgements

ChatGPT platform for minor paraphrasing and proofreading parts of the manuscript.

References

1 M. N. Singh, K. S. Y. Hemant, M. Ram and H. G. Shivakumar, *Results Pharma Sci.*, 2010, **5**, 65–77.

2 J. L. de Oliveira, E. V. R. Campos, M. Bakshi, P. C. Abhilash and L. F. Fraceto, *Biotechnol. Adv.*, 2014, **32**, 1550–1561.

3 S. J. Risch, *Encapsulation and Controlled Release of Food Ingredients*, 1995.

4 V. Nedovic, A. Kalusevic, V. Manojlovic, S. Levic and B. Bugarski, *Procedia Food Sci.*, 2011, **1**, 1806–1815.

5 A. Ammala, *Int. J. Cosmet. Sci.*, 2013, **35**, 113–124.

6 M. Saifullah, M. R. I. Shishir, R. Ferdowsi, M. R. Tanver Rahman and Q. Van Vuong, *Trends Food Sci. Technol.*, 2019, **86**, 230–251.

7 K. Li, X. Cheng, F. Zhu, L. Li, Z. Xie, H. Luan, Z. Wang, Z. Ji, H. Wang, F. Liu, Y. Xue, C. Jiang, X. Feng, L. Li, J. A. Rogers, Y. Huang and Y. Zhang, *Adv. Funct. Mater.*, 2019, **29**, 1–12.

8 S. J. Risch, *Encapsulation and Controlled Release of Food Ingredients*, 1995, vol. 590, pp. 2–7.

9 B. Wu, C. Yang, B. Li, L. Feng, M. Hai, C. Zhao, D. Chen, K. Liu and D. A. Weitz, *Small*, 2020, **16**, 2002716.

10 Y. Niu, J. Wu, Y. Kang, Q. Zhao, Z. Xiao and D. Zhao, *Prog. Org. Coat.*, 2023, **176**, 107390.

11 N. Mehta, P. Kumar, A. K. Verma, P. Umaraw, Y. Kumar, O. P. Malav, A. Q. Sazili, R. Domínguez and J. M. Lorenzo, *Appl. Sci.*, 2022, **12**, 1–34.

12 E. Kwizera, S. Stewart, M. M. Mahmud and X. He, *J. Heat Transfer*, 2022, **144**(3), 030801.

13 Q. Du, C. Zhang, S. Sun, Y. Wang, H. Liu, Y. Wei and Y. Jiang, *Langmuir*, 2020, **36**(47), 14318–14323, DOI: **10.1021/acs.langmuir.0c02582**.

14 C. Comanescu, *Chemistry*, 2022, **4**, 872–930.

15 A. Nacev, C. Beni, O. Bruno and B. Shapiro, *Nanomedicine*, 2010, **5**, 1459–1466.

16 L. Agiotis, I. Theodorakos, S. Samothrakitis, S. Papazoglou, I. Zergioti and Y. S. Raptis, *J. Magn. Magn. Mater.*, 2016, **401**, 956–964.

17 T. Neuberger, B. Schöpf, H. Hofmann, M. Hofmann and B. Von Rechenberg, *J. Magn. Magn. Mater.*, 2005, **293**, 483–496.

18 R. Hiergeist, W. Andrak, N. Buske, R. Hergt, I. Hilger, U. Richter and W. Kaiser, *J. Magn. Magn. Mater.*, 1999, **201**, 420–422.

19 P. E. Feuser, L. D. S. Bubniak, M. C. D. S. Silva, A. D. C. Viegas, A. Castilho Fernandes, E. Ricci-Junior, M. Nele, A. C. Tedesco, C. Sayer and P. H. H. De Araújo, *Eur. Polym. J.*, 2015, **68**, 355–365.

20 J. Huang, W. Huang, Y. Chen, Y. S. Zhang, J. Zhong, Y. Li and J. Zhou, *RSC Adv.*, 2018, **8**, 41956–41965.

21 Q. Wang, S. Liu, F. Yang, L. Gan, X. Yang and Y. Yang, *Int. J. Nanomed.*, 2017, **12**, 4335–4347.

22 M. Latikka, M. Backholm, J. V. I. Timonen and R. H. A. Ras, *Curr. Opin. Colloid Interface Sci.*, 2018, **36**, 118–129.

23 C. Scherer and A. M. F. Neto, *Braz. J. Phys.*, 2005, **35**, 718–727.

24 R. Beig, W. Domcke, B.-G. Englert, U. Frisch, P. Hanggi, G. Hasinger, K. Hepp, W. Hillebrandt, D. Imboden, R. L. Jaffe, R. Lipowsky, H. v Lohneysen, I. Ojima, D. Sornette, S. Theisen, W. Weise, J. Wess and J. Zittartz, *Ferrofluids – Magnetically Controllable Fluids and Their Applications*, 2002.

25 U. Banerjee, S. Misra and S. K. Mitra, *Adv. Mater. Interfaces*, 2022, **9**, 2200288.

26 C. Wischnewski, E. Zwar, H. Rehage and J. Kierfeld, *Langmuir*, 2018, **34**(45), 13534–13543, DOI: **10.1021/acs.langmuir.8b02357**.

27 Z. Liu, J. Liu, X. Cui, X. Wang, L. Zhang and P. Tang, *Front. Media S.A.*, 2020, **8**, 124.

28 Z. Chen, S. Song, J. Ma, S. Da Ling, Y. D. Wang, T. T. Kong and J. H. Xu, *Chem. Eng. Sci.*, 2022, **248**, 117216.

29 B. Farasati Far, M. Safaei, R. Nahavandi, A. Gholami, M. R. Naimi-Jamal, S. Tamang, J. E. Ahn, M. Ramezani Farani and Y. S. Huh, *ACS Omega*, 2024, **9**(27), 29139–29158.

30 D. K. Nguyen, Y. M. Son and N. E. Lee, *Adv. Healthcare Mater.*, 2015, **4**, 1537–1544.

31 Y. He, J. Tang, Y. Hu, S. Yang, F. Xu, M. Zrínyi and Y. Mei Chen, *Chem. Eng. J.*, 2023, **462**, 142193.

32 F. Gang, L. Jiang, Y. Xiao, J. Zhang and X. Sun, *Nano Sel.*, 2021, **2**, 2291–2307.

33 I. Singh, C. S. Lacko, Z. Zhao, C. E. Schmidt and C. Rinaldi, *J. Colloid Interface Sci.*, 2020, **561**, 647–658.

34 Y. Li, G. Huang, X. Zhang, B. Li, Y. Chen, T. Lu, T. J. Lu and F. Xu, *Adv. Funct. Mater.*, 2013, **23**, 660–672.

35 Z. Xu, Z. Wu, M. Yuan, Y. Chen, W. Ge and Q. Xu, *iScience*, 2023, **26**(5), 106727.

36 D. K. Hwang, D. Dendukuri and P. S. Doyle, *Lab Chip*, 2008, **8**, 1640–1647.

37 Z. Yang, S. Jin, C. Zhang, J. Ren, W. Jing and X. Wei, *Chem. Eng. Sci.*, 2023, **281**, 119082.

38 Y. He, J. Tang, Y. Hu, S. Yang, F. Xu, M. Zrínyi and Y. Mei Chen, *Chem. Eng. J.*, 2023, **462**, 142193.

39 S. Mitra, N. S. K. Gunda, S. Misra and K. Trinavee, Liquid encapsulation method and compositions and uses related thereto, 12145120, 2020.

40 M. R. Gunjan, U. Banerjee, S. Misra and S. K. Mitra, *Adv. Mater. Interfaces*, 2023, **10**, 2300144.

41 S. Misra, K. Trinavee, N. S. K. Gunda and S. K. Mitra, *J. Colloid Interface Sci.*, 2019, **558**, 334–344.

42 S. Misra, U. Banerjee and S. K. Mitra, *ACS Appl. Mater. Interfaces*, 2023, **15**, 23938–23950.

43 P. Degen, E. Zwar, I. Schulz and H. Rehage, *J. Phys.: Condens. Matter*, 2015, **27**, 194105.

44 P. Degen, S. Leick, F. Siedenbiedel and H. Rehage, *Colloid Polym. Sci.*, 2012, **290**, 97–106.

45 U. Banerjee, S. Misra and S. K. Mitra, *J. Colloid Interface Sci.*, 2025, **679**, 1266–1276.

46 R. E. Rosensweig, *Ferrohydrodynamics*, Dover Publications, 2014.

47 P.-G. de Gennes, F. Brochard-Wyart and D. Quéré, *Capillarity and Wetting Phenomena*, Springer, New York, 2004.

48 C. Rigoni, M. Pierno, G. Mistura, D. Talbot, R. Massart, J. C. Bacri and A. Abou-Hassan, *Langmuir*, 2016, **32**, 7639–7646.